ARCHIVES OF ELECTRICAL ENGINEERING VOL. 72(1), pp. 189–210 (2023)

DOI 10.24425/aee.2023.143697

Armature MMF and electromagnetic performance analysis of dual three-phase 10-pole/24-slot permanent magnet synchronous machine

ZHENFEI CHEN[1] ✉, NING XING[2], HONGZHONG MA[1], ZHIXIN LI[3], JIAYU LI[1], CHENYANG FAN[1]

[1] *College of Energy and Electrical Engineering, Hohai University Jiangsu, China*

[2] *School of Electrical and Information Engineering, Tianjin University Tianjin, China*

[3] *Electric Power Science Research Institute, Jiangsu Electric Power Company Jiangsu, China*

e-mail: ✉*chenzhenfei@hhu.edu.cn, 1292983488@qq.com*

(Received: 23.07.2022, revised: 09.11.2022)

Abstract: Fractional-slot concentrated-winding permanent magnet synchronous machines (FSCW-PMSMs) have a good prospect of application in the drive system of electric and hybrid electric vehicles. However, the armature magnetomotive force (MMF) of FSCW-PMSM contains a large number of space harmonics, which induce large magnet eddy-current loss (ECL). To solve this problem, a dual three-phase 10-pole and 24-slot winding layout is proposed. MMF harmonic analysis shows that the 1st, 7th and 17th space-harmonic winding factors of the proposed winding can be reduced by 100%, 87% and 87% respectively, compared with a dual three-phase 10-pole and 12-slot winding. Electromagnetic performances of the proposed machine under rated sinusoidal current supply and space vector pulse-width-modulated (SVPWM) voltage supply are investigated based on 2D finite-element analysis. It is shown that the proposed machine can meet the requirement of torque and efficiency in the full speed range. Especially, magnet ECL can be reduced greatly due to the reduction of the 7th and 17th space harmonics.

Key words: dual three-phase winding, fractional-slot concentrated-winding permanent magnet synchronous machines (FSCW-PMSMs), MMF harmonic analysis, space harmonics, magnet eddy-current loss (ECL), SVPWM voltage supply

1. Introduction

In the drive system of electric vehicles (EVs) and hybrid electric vehicles (HEVs), PMSMs have higher efficiency and torque density than induction machines and switched reluctance machines [1–4]. Many researchers are devoted to designing the PMSM with superior performance. The suggestions for optimization implementation on the transient and steady-state performance of the line-start PMSM (LSPMSM), which can start direct-on-line, are presented in [5, 6]. Some critical design areas such as materials, topology design, thermal management and an optimization approach to the performance of the PMSM for EVs, are highlighted in [7]. A generalized design for the optimal choice of permanent magnet-assisted synchronous reluctance motors (PMa-SynRMs) for traction motors is presented in [8]. In terms of winding layouts, compared with integral-slot distributed-winding PMSMs (ISDW-PMSMs), FSCW-PMSMs have the advantages of short end-windings, a high slot-fill factor, low cogging torque and high fault tolerance [9, 10]. Thus, FSCW-PMSMs have a good prospect in the electric drive system.

However, different from ISDW-PMSMs, the order of the fundamental armature MMF of FSCW-PMSMs is p, which is equal to the magnet pole-pair number. The space harmonics with orders lower than p are called sub-harmonics, while the other space harmonics with orders higher than p are called super-harmonics. The super-harmonics with the same winding factor as the fundamental component are also called slot harmonics [11]. These space harmonics rotate with the rotor asynchronously, which will induce large magnet ECL. Due to the poor heat dissipation condition of the rotor, temperature rise caused by ECL will lead to irreversible demagnetization and even damage the machines [12, 13].

To solve this problem, many researchers put forward many methods. One kind of method is to optimize machine structure. The use of magnetic flux barriers in the stator core can suppress the sub-harmonics of air-gap flux density [14, 15]. However, it will make the manufacturing complex and it is not suitable for the machines with heavy load conditions. Magnet segmentation is used to cut off eddy current and reduce ECL [16]. However, it will increase the manufacturing cost and it is not suitable for the machines with short axial length. The other kind of method is to optimize winding layouts. The winding coils with unequal turns per coil side, a multi-layer winding and a dual three-phase winding are used to reduce the sub-harmonics, but it is not effective on slot harmonics [17–23]. Recently, some researchers use stator shifting to reduce a certain slot harmonic [24–28]. The slot harmonic and sub-harmonic can be reduced at the same time when FSCW-PMSMs combine stator shifting and a dual three-phase winding.

In this paper, a dual three-phase 10-pole/24-slot winding layout of low space harmonics is proposed. In section 2, the armature MMF of a three-phase 10-pole/12-slot, dual three-phase 10-pole/12-slot, three-phase 10-pole/24-slot and the proposed dual three-phase 10-pole/24-slot PMSMs are derived, and armature MMF harmonic analysis is carried out. In section 3, electromagnetic performances of the four machines under rated sinusoidal current supply are investigated, such as torque, losses, electromagnetic efficiency and magnet space-harmonic ECL. In section 4, electromagnetic performances under SVPWM voltage supply are investigated, such as torque, efficiency in the full speed range, losses under maximum-torque-per-ampere (MTPA) control and magnet time- and space-harmonic ECL. In section 5, some main conclusions are summarized.

2. Armature MMF harmonic analysis of the proposed 10-pole/24-slot winding

2.1. 10-pole/12-slot winding layout

The winding layouts of three-phase and dual three-phase 10-pole/12-slot PMSMs are shown in Fig. 1. The symbols and reference directions of the corresponding coils are also shown in Fig. 1.

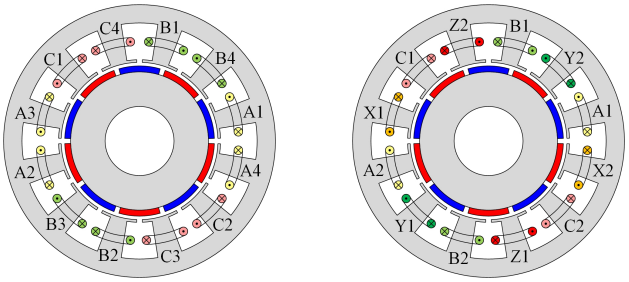

(a) (b)

Fig. 1. Winding layouts of 10-pole/12-slot PMSM: three-phase winding (a); dual three-phase winding (b)

The armature MMF distribution of phase A of the three-phase 10-pole/12-slot PMSM with the mechanical angle θ is shown in Fig. 2, where N_{c12S} is the number of turns per coil, i is the armature current, and $N_{c12S}i$ is the amplitude of MMF.

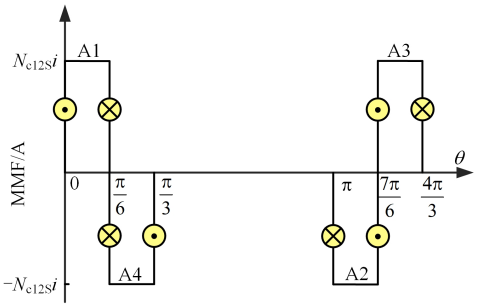

Fig. 2. Armature MMF distribution of phase A of three-phase 10-pole/12-slot PMSM

The Fourier series of MMF of coil group A1, A2, B1, B2 and C1, C2 is calculated as

$$F_{1p}(\theta,t)=\sum_{k=1,-5,7,\ldots}^{\infty}\frac{6N_{c12S}I_m}{k\pi}\sin\left(\frac{k\pi}{12}\right)\sin(\omega t-k\theta), \tag{1}$$

where: k is the order of space harmonic, I_m is the amplitude of armature current, ω is the electrical angular velocity. $\sin\left(\frac{k\pi}{12}\right)$ is the pitch factor caused by the short-pitched coil.

The MMF of coil group A3, A4, B3, B4 and C3, C4 is calculated as

$$F_{2p}(\theta,t) = -\sum_{k=1,-5,7,\ldots}^{\infty} \frac{6N_{c12S}I_m}{k\pi} \sin\left(\frac{k\pi}{12}\right) \sin\left[\omega t - k\left(\theta - \frac{\pi}{6}\right)\right]. \tag{2}$$

The total armature MMF of the three-phase 10-pole/12-slot PMSM can be calculated by (1) and (2).

$$\begin{aligned} F_{c12S}(\theta,t) &= F_{1p}(\theta,t) + F_{2p}(\theta,t) \\ &= -\sum_{k=1,-5,7,\ldots}^{\infty} \frac{12N_{c12S}I_m}{k\pi} \sin\left(\frac{k\pi}{12}\right) \sin\left(\frac{k\pi}{12}\right) \cos\left[\omega t - k\theta + \frac{k\pi}{12}\right], \end{aligned} \tag{3}$$

where the harmonics of order 5, 11, 17, $\ldots, 6v-1$ ($v = 1, 2, 3, \ldots$) rotate in the same direction of the rotor while the harmonics of order $1, 7, 13, \ldots, 6v+1$ ($v = 0, 1, 2, \ldots$) rotate in the opposite direction. The other expression of $\sin\left(\frac{k\pi}{12}\right)$ is the distribution factor caused by the distributed coils per phase.

The k-th space-harmonic winding factor W_{TP12Sk} is the product of the pitch factor and distribution factor, as shown in (4).

$$W_{TP12Sk} = \sin\left(\frac{k\pi}{12}\right) \sin\left(\frac{k\pi}{12}\right). \tag{4}$$

For the dual three-phase 10-pole/12-slot PMSM, phases A, B, C and phases X, Y, Z are supplied with two groups of three-phase current with a phase shift of 30°. The MMF of coil group X1, X2, Y1, Y2 and Z1, Z2 is calculated as

$$F_{2p\_DTP12S}(\theta,t) = -\sum_{k=1,-5,7,\ldots}^{\infty} \frac{6N_{c12S}I_m}{k\pi} \sin\left(\frac{k\pi}{12}\right) \sin\left[\left(\omega t - \frac{\pi}{6}\right) - k\left(\theta - \frac{\pi}{6}\right)\right]. \tag{5}$$

The total armature MMF of the dual three-phase 10-pole/12-slot PMSM can be calculated based on (3) and (5).

$$F_{DTP12S}(\theta,t) = -\sum_{k=1,-5,7,\ldots}^{\infty} \frac{12N_{c12S}I_m}{k\pi} \sin\left(\frac{k\pi}{12}\right) \sin\left[\frac{(k-1)\pi}{12}\right] \cos\left[\omega t - k\theta + \frac{(k-1)\pi}{12}\right]. \tag{6}$$

The k-th space-harmonic winding factor $W_{DTP12Sk}$ is

$$W_{DTP12Sk} = \sin\left(\frac{k\pi}{12}\right) \sin\left[\frac{(k-1)\pi}{12}\right]. \tag{7}$$

2.2. The proposed 10-pole/24-slot winding layout

The winding layouts of three-phase and the proposed dual three-phase 10-pole/24-slot PMSMs are shown in Fig. 3.

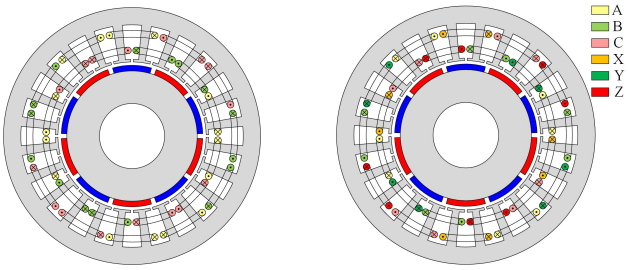

(a) (b)

Fig. 3. Winding layouts of 10-pole/24-slot PMSM: three-phase winding (a); the proposed dual three-phase winding (b)

Based on (3), the MMF of the top-layer winding group near the air gap is calculated as

$$F_{\mathrm{t\_TP24S}}(\theta,t) = -\sum_{k=1,-5,7,\ldots}^{\infty} \frac{12N_{\mathrm{c24S}}I_{\mathrm{m}}}{k\pi} \sin\left(\frac{k\pi}{12}\right) \sin\left(\frac{k\pi}{12}\right) \cos\left[\omega t - k\theta + \frac{k\pi}{12}\right], \tag{8}$$

where: N_{c24S} is the number of turns per coil of the 10-pole/24-slot PMSM.

The MMF of the bottom-layer winding group near the stator yoke is calculated as

$$F_{\mathrm{b\_TP24S}}(\theta,t) = -\sum_{k=1,-5,7,\ldots}^{\infty} \frac{12N_{\mathrm{c24S}}I_{\mathrm{m}}}{k\pi} \sin\left(\frac{k\pi}{12}\right) \sin\left(\frac{k\pi}{12}\right) \cos\left[\omega t - k\theta + \frac{k\pi}{2}\right]. \tag{9}$$

The total armature MMF of the three-phase 10-pole/24-slot PMSM can be calculated by (8) and (9).

$$\begin{aligned} F_{\mathrm{TP24S}}(\theta,t) &= F_{\mathrm{t\_TP24S}}(\theta,t) + F_{\mathrm{b\_TP24S}}(\theta,t) \\ &= -\sum_{k=1,-5,7,\ldots}^{\infty} \frac{24N_{\mathrm{c24S}}I_{\mathrm{m}}}{k\pi} \sin\left(\frac{k\pi}{12}\right) \sin\left(\frac{k\pi}{12}\right) \cos\left(\frac{5k\pi}{24}\right) \cos\left[\omega t - k\theta + \frac{7k\pi}{2}\right]. \end{aligned} \tag{10}$$

The k-th space-harmonic winding factor $W_{\mathrm{TP24S}k}$ is

$$W_{\mathrm{TP24S}k} = \sin\left(\frac{k\pi}{12}\right) \sin\left(\frac{k\pi}{12}\right) \cos\left(\frac{5k\pi}{24}\right). \tag{11}$$

Based on (3), (6), (8) and (9), the armature MMF of the proposed dual three-phase 10-pole/24-slot PMSM is calculated as

$$\begin{aligned} F_{\mathrm{DTP24S}}(\theta,t) = &-\sum_{k=1,-5,7,\ldots}^{\infty} \frac{24N_{\mathrm{c24S}}I_{\mathrm{m}}}{k\pi} \\ &\cdot \sin\left(\frac{k\pi}{12}\right) \sin\left[\frac{(k-1)\pi}{12}\right] \cos\left(\frac{5k\pi}{24}\right) \cos\left[\omega t - k\theta + \frac{(k-1)\pi}{12} + \frac{5k\pi}{24}\right]. \end{aligned} \tag{12}$$

The k-th space-harmonic winding factor $W_{\mathrm{DTP24S}k}$ is

$$W_{\mathrm{DTP24S}k} = \sin\left(\frac{k\pi}{12}\right)\sin\left[\frac{(k-1)\pi}{12}\right]\cos\left(\frac{5k\pi}{24}\right). \tag{13}$$

Based on (3), (6), (10) and (12), when I_{m} is 18.38 A, N_{c12S} is 192 and N_{c24S} is 96, the armature MMF distribution and harmonic spectra of the proposed three-phase 10-pole/12-slot PMSM, dual three-phase 10-pole/12-slot PMSM and three-phase 10-pole/24-slot PMSM are shown in Fig 4. Based on (4), (7), (11) and (13), the space-harmonic winding factor is shown in Table 1. The four machines are denoted as DTP-24S, TP-12S, DTP-12S and TP-24S, respectively.

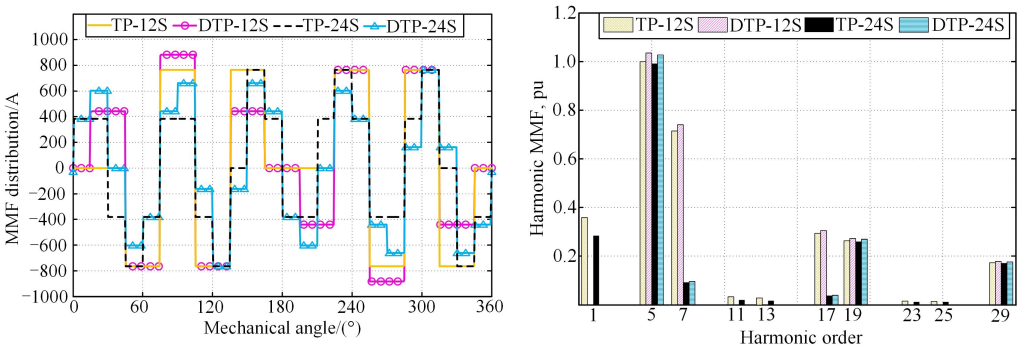

(a) (b)

Fig. 4. Armature MMF distribution and harmonic spectra of the four machines: MMF distribution (a); harmonic spectra (b)

It can be seen from Fig. 4 and Table 1 that the space-harmonic winding factor of order 1 and $11, 13, \ldots, 12v \pm 1$ ($v = 1, 2, 3, \ldots$) of DTP-24S becomes 0. The fundamental winding factor of DTP-24S is 2.65% higher than that of TP-12S, 3.57% higher than that of TP-24S and only 0.85% lower than that of DTP-12S. The 7th and 17th space-harmonic winding factor is 86.49% lower than that of TP-12S and 86.95% lower than that of DTP-12S.

The methodology flow chart for comparative study of the four machines is shown in Fig. 5.

Table 1. Space-harmonic winding factor

k	TP-12S	DTP-12S	TP-24S	DTP-24S
1	0.067	0	0.053	0
5	0.933	0.966	0.925	0.958
7	0.933	0.966	0.122	0.126
11	0.067	0	0.041	0
13	0.067	0	0.041	0
17	0.933	0.966	0.122	0.126
19	0.933	0.966	0.925	0.958

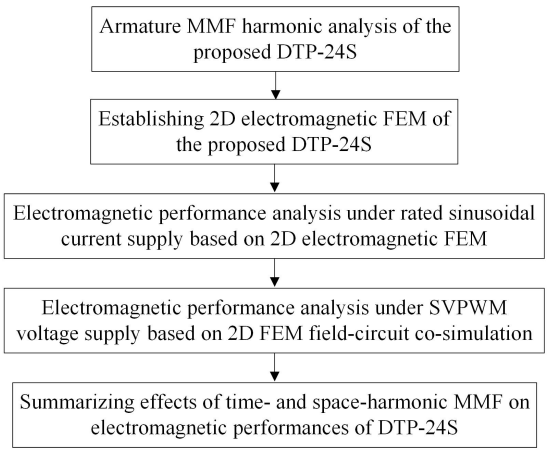

Fig. 5. Methodology flow chart for comparative study

3. Electromagnetic performances under rated sinusoidal current supply

In this section, 2D electromagnetic finite-element models (FEMs) of TP-12S, DTP-12S, TP-24S and DTP-24S are established in AnsysEM Maxwell, as shown in Fig. 6. Electromagnetic performances of the four machines under rated sinusoidal current supply are investigated based on the 2D FEMs. Besides, magnet space-harmonic ECL is calculated by average eddy-current

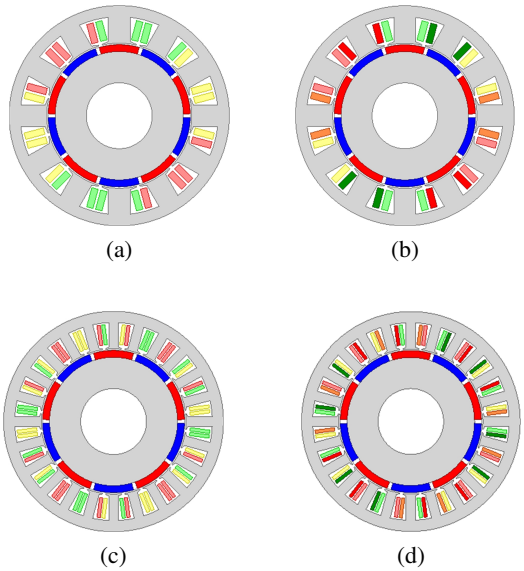

Fig. 6. 2D electromagnetic FEMs of the four machines: TP-12S (a); DTP-12S (b); TP-24S (c); DTP-24S (d)

density of all mesh elements, which is used to investigate the effects of space harmonics on magnet ECL. The four machines have the same basic parameters but different winding parameters, as shown in Table 2 and Table 3.

Table 2. Basic parameters of the four machines

Parameter name	**Value**	**Unit**
Rated speed	1 500	r/min
Rated current	13	A
Stator inner diameter	110	mm
Stator outer diameter	167	mm
Slot inner diameter	113.6	mm
Slot outer diameter	150	mm
Axial length	70	mm
Air-gap length	1.15	mm
Magnet thickness	5.2	mm
Magnet conductivity	625 000	S/m
Magnet pole arc	0.91	–

Table 3. Winding parameters of the four machines

Parameter name	**TP-12S**	**DTP-12S**	**TP-24S**	**DTP-24S**
Pole/slot	10/12	10/12	10/24	10/24
Slot width/mm	13.2	13.2	7.5	7.5
Slot area/mm^2	339	339	189	189
Wire diameter/mm	1	1	1	1
Turns/slot	192	192	96	96
Parallel branches	2	2	2	2
Turns/phase	192	192	192	192
Slot fill factor	44%	44%	40%	40%

To ensure the same turns-in-series per phase of 10-pole/12-slot and 10-pole/24-slot PMSMs, the turns per slot are set to 192 and 96.

3.1. No-load line back-EMF and on-load magnetic field

Figure 7 shows the 2D FEM-calculated no-load line back-EMF of the four machines and Table 4 shows the harmonic contents. It can be seen that the total harmonic distortion (THD) of no-load line back-EMF of DTP-24S is lower than that of TP-12S and DTP-12S.

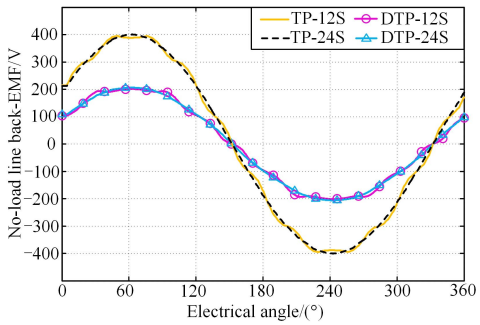

Fig. 7. 2D FEM-calculated no-load line back-EMF of the four machines

Table 4. Harmonic contents of no-load line back-EMF of the four machines

Harmonic order	**Amplitude/V**			
	TP-12S	**DTP-12S**	**TP-24S**	**DTP-24S**
1	397.97	205.91	398.66	206.15
3	0	0	0	0
5	2.17	4.78	1.17	1.93
7	2.43	4.32	1.14	2.04
9	0	0	0	0
11	14.36	7.71	0.19	0.26
THD/%	3.94	5.07	0.63	1.44

Figure 8 shows the 2D FEM-calculated on-load magnetic field of the four machines under rated conditions. It can be seen that the maximum flux density of the stator yoke and stator teeth of DTP-24S is greater than that of TP-12S and DTP-12S due to the reduction of the stator teeth width.

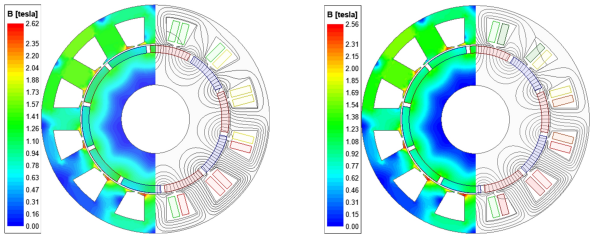

(a) (b)

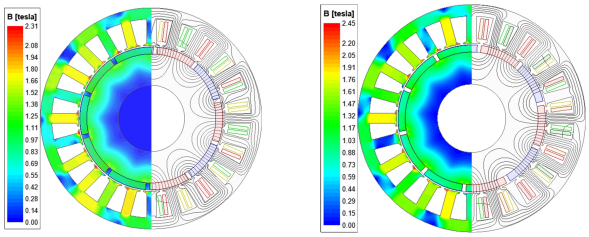

(c) (d)

Fig. 8. On-load magnetic field of the four machines: TP-12S (a); DTP-12S (b); TP-24S (c); DTP-24S (d)

3.2. Torque characteristics

Figure 9(a) shows the 2D FEM-calculated electromagnetic torque of the four machines under rated conditions and $i_d = 0$ control. $i_d = 0$ control refers to the armature current being in phase with no-load phase back-EMF and electromagnetic torque reaching the maximum. Figure 9(b) shows the cogging torque of the 10-pole/24-slot PMSM and 10-pole/12-slot PMSM. Table 5 shows the corresponding torque characteristics.

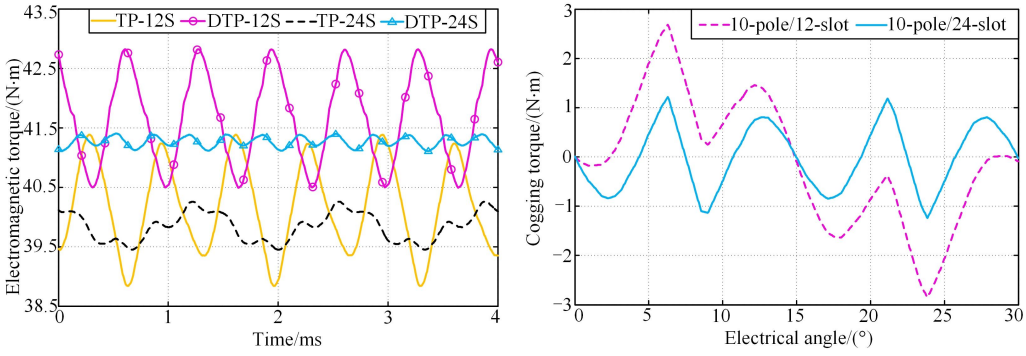

(a) (b)

Fig. 9. FEM-calculated electromagnetic torque of the four machines: electromagnetic torque (a); cogging torque (b)

Table 5. Analysis of torque characteristics

Parameter name	TP-12S	DTP-12S	TP-24S	DTP-24S
T_{ave}/(N·m)	40.18	41.66	39.84	41.27
$\Delta T_{peak-peak}$/(N·m)	2.55	2.33	0.81	0.3
T_{ripple}/%	3.17	2.80	1.02	0.36
$T_{cogging}$/(N·m)	5.61	5.61	2.28	2.28

The average electromagnetic torque of DTP-24S is 3.59% higher than that of TP-24S, 2.71% higher than that of TP-12S and 0.94% lower than that of DTP-12S. The torque ripple of DTP-24S is the lowest due to the lowest space-harmonic contents. In addition, the cogging torque of the 10-pole/24-slot PMSM is lower than that of the 10-pole/12-slot PMSM because the 10-pole/24-slot PMSM has a smaller least common multiple (LCM) of the pole number and slot number.

3.3. Losses and electromagnetic efficiency

The AC copper loss considering skin and proximity effect is calculated by the 2D magnetic eddy-current solver. Each conductor in the slots is modelled separately and the ohmic loss density distribution of conductors is shown in Fig. 10. The conductors close to the slot opening are greatly affected by skin and proximity effect, and the ohmic loss density distribution is uneven. The closer the conductors are to the slot body bottom, the less are affected by skin and proximity effect. The AC copper loss can be calculated by the volume integral of ohmic loss density over the conductors.

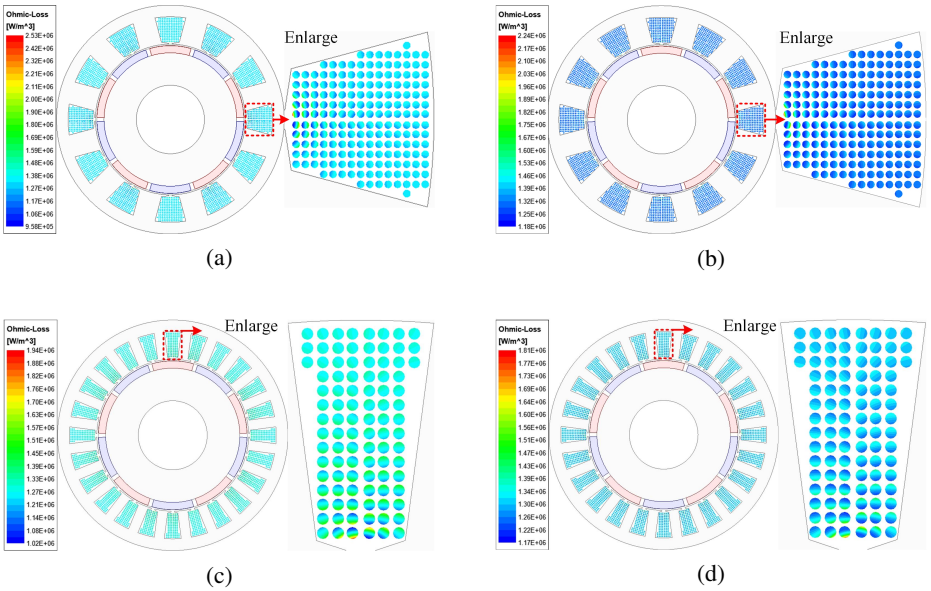

Fig. 10. Ohmic loss density distribution of conductors at 1 500 r/min under rated sinusoidal current supply: TP-12S (a); DTP-12S (b); TP-24S (c); DTP-24S (d)

The stator core loss, magnet ECL and rotor core loss are calculated by the 2D FEM using the magnetic transient solver. The output power can be calculated by average electromagnetic torque and rotor speed, as shown in (14). The friction and windage losses of the four machines are ignored in the comparative study. So, the electromagnetic efficiency is calculated by (15).

$$p_{\text{out}} = T_{\text{ave}} \cdot \frac{2\pi n_{\text{r}}}{60}, \tag{14}$$

$$\eta = \frac{p_{\text{out}}}{p_{\text{out}} + p_{\text{mag}} + p_{\text{ACcu}} + p_{\text{score}} + p_{\text{rcore}}}, \tag{15}$$

where n_{r} is the rotor speed. p_{ACcu} is the AC copper loss. p_{score} is the stator core loss. p_{rcore} is the rotor core loss.

The FEM-calculated losses, output power and electromagnetic efficiency of the four machines under rated conditions are shown in Table 6.

Table 6. FEM-calculated losses, output power and efficiency of the four machines

Parameter name	TP-12S	DTP-12S	TP-24S	DTP-24S
p_{mag}/W	46.38	45.47	5.92	4.53
p_{ACcu}/W	157.66	157.70	157.33	157.36
p_{score}/W	88.35	88.17	117.15	117.13
p_{rcore}/W	1.22	0.82	0.61	0.34
p_{total}/W	293.61	292.16	281.02	279.36
p_{out}/W	6 311.46	6 543.94	6 258.05	6 482.68
η/%	95.55	95.73	95.70	95.87

The stator core loss of DTP-24S is 24.57% higher than TP-12S and 24.72% higher than DTP-12S because flux density of the stator teeth and stator yoke increases. The magnet ECL of DTP-24S is 90.23% lower than TP-12S and 90.04% lower than DTP-12S. The efficiency of DTP-24S is 0.34% higher than TP-12S and 0.15% higher than DTP-12S.

3.4. Magnet space-harmonic ECL

From (3), the mechanical angular velocity of k-th space-harmonic MMF is ω/k in the stator reference frame. In the rotor reference frame, it can be calculated as

$$\omega_{kr} = \left(\frac{\omega}{\text{sgn} \cdot k} - \frac{\omega}{p}\right), \tag{16}$$

where sgn is equal to 1 when the k-th space harmonic rotates in the same direction of the rotor, while sgn is equal to -1 when the k-th space harmonic rotates in the opposite direction.

The frequency of the k-th space-harmonic MMF in the rotor reference frame is

$$f_{kr} = \frac{\omega}{2\pi}\left|\text{sgn} - \frac{k}{p}\right|. \tag{17}$$

Table 7 shows the sgn and f_{kr} of the space-harmonic MMF in the rotor reference frame at 1 500 r/min.

Magnet mesh generation of DTP-24S can be obtained based on the 2D FEM, as shown in Fig. 11(a). When the machine runs at 1 500 r/min, the average eddy-current density of an element during the rotor rotation period is shown in Fig. 11(b).

Table 7. The sgn and f_{kr} of space-harmonic MMF under rated sinusoidal current

k	sgn	f_{kr} [Hz]
1	−1	150
5	1	0
7	−1	300
11	1	150
13	−1	450
17	1	300
19	−1	600

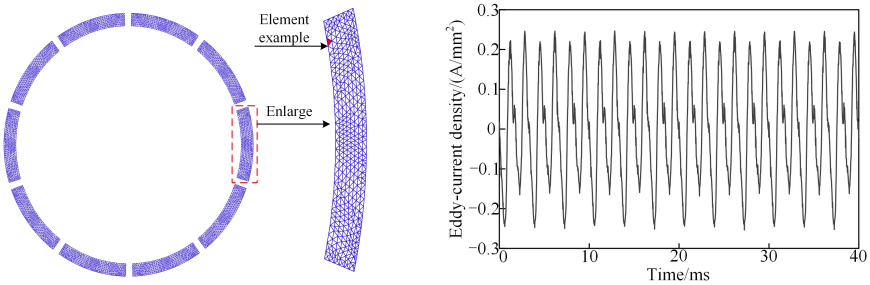

(a) (b)

Fig. 11. Magnet mesh generation and average eddy current density of an element of DTP-24S at 1 500 r/min: mesh generation (a); average eddy-current density (b)

The average eddy-current density distribution $J_{\text{ave}_i}(t)$ of the i-th mesh element can be expanded into Fourier series

$$J_{\text{ave}i}(t) = \sum_n J_{\text{in}} \cos\left(n\omega t + \varphi_{\text{in}}\right), \tag{18}$$

where n is the harmonic order of the Fourier series. J_{in} and φ_{in} are the amplitude and phase of n-th harmonic eddy-current density.

Magnet space-harmonic ECL can be calculated by Ohm's law and the Fourier series of the average eddy-current density of all mesh elements, as shown in (19).

$$p_{\text{mag}}(n) = \frac{p l_{\text{a}}}{\sigma} \sum_{i=1}^{N_{\text{m}}} S_i J_{\text{in}}^2, \tag{19}$$

where: $p_{\text{mag}}(n)$ is the n-th space-harmonic ECL, l_{a} is the axial length, σ is the conductivity, N_{m} is the number of mesh elements and S_i is the area of the i-th mesh element.

Figure 12 shows the space-harmonic ECL of the four machines calculated by (19) under rated sinusoidal current supply.

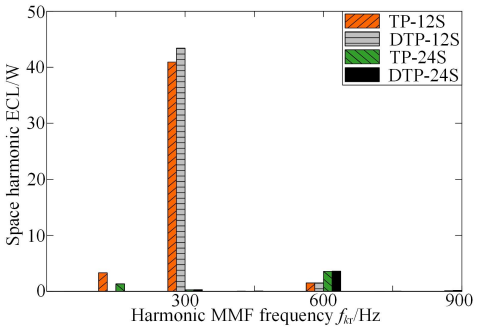

Fig. 12. Magnet space-harmonic ECL of the four machines under rated sinusoidal current supply

It can be seen from Fig. 12 and Table 7 that the frequency of harmonic eddy-current density corresponds to that of space-harmonic MMF in the rotor reference frame. The 300 Hz harmonic ECL accounts for 90.75%, 94.73%, 2.21% and 2.81% of the total ECL in TP-12S, DTP-12S, TP-24S and DTP-24S, respectively. The 300 Hz harmonic ECL of DTP-24S is 99.70% lower than that of TP-12S and DTP-12S due to the low amplitude of the 7th and 17th space-harmonic MMF.

4. Electromagnetic performances under SVPWM voltage supply

In this section, the torque, phase RMS voltage and efficiency of the four machines in the full-speed range are investigated. The losses of the four machines at the turning speed under SVPWM voltage supply and MTPA control are calculated by 2D FEM field-circuit co-simulation established in Ansys Maxwell and Simplorer. Besides, the magnet time- and space-harmonic ECL of DTP-12S and DTP-24S is calculated and contrasted by using (19).

4.1. Torque characteristics and efficiency in full speed range

The 2D FEM field-circuit co-simulation block diagram for the full-speed range of DTP-24S is shown in Fig. 13, which is based on double d-q transformation. The flux weakening angle β is equal to the difference between $\frac{u_{\mathrm{dc}}}{\sqrt{3}}$ and $\sqrt{u_{\mathrm{d1}}^2 + u_{\mathrm{q1}}^2}$ or $\sqrt{u_{\mathrm{d2}}^2 + u_{\mathrm{q2}}^2}$ after amplified by the PI regulator. When the difference is higher than zero, β is equal to 0 rad, then i_{d1r} and i_{d2r} are 0 A, the control block diagram realizes $i_{\mathrm{d}} = 0$ or MTPA control. When the difference is lower than zero, β is lower than 0 rad, then i_{d1r} and i_{d2r} are lower than 0 A, the control block diagram realizes flux-weakening control.

The control block diagram for the full-speed range of the three-phase PMSM can be easily realized by $d-q$ transformation, which only considers d1 and q1 components in Fig. 13. It can be seen from Table 4 that the required dc-link voltage u_{dc} of the three-phase PMSM is approximately twice as much as that of the dual three-phase PMSM to ensure an equal power density.

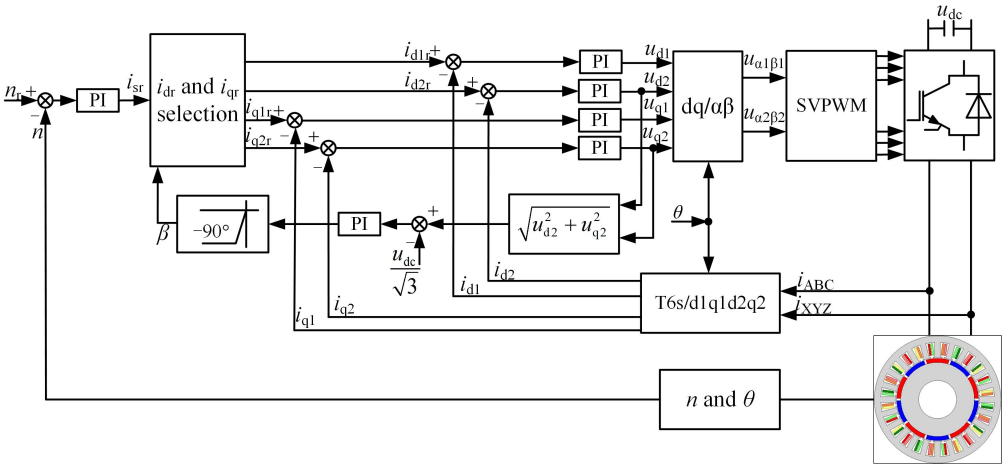

Fig. 13. 2D FEM field-circuit co-simulation block diagram for full speed range of DTP-24S

The u_{dc} of TP-12S and TP-24S is set to 420V and the u_{dc} of DTP-12S and DTP-24S is set to 210 V. Within the limit of rated current, the output torque and phase back-EMF of the four machines in the full-speed range are calculated by the 2D FEM, as shown in Fig. 14.

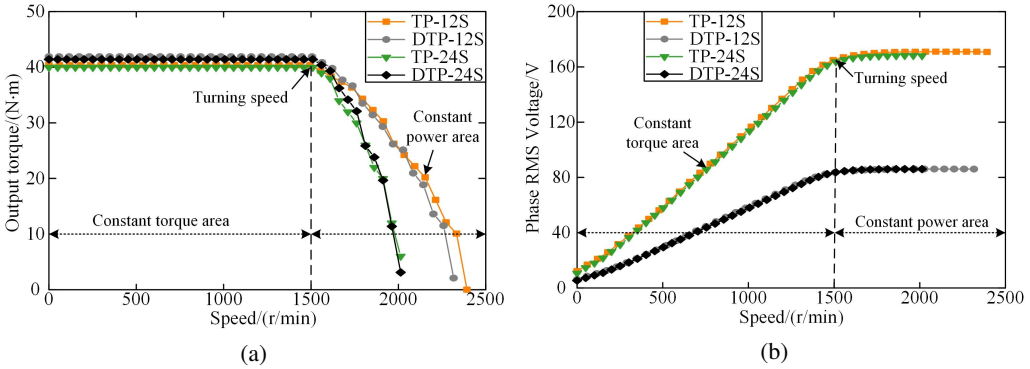

Fig. 14. Torque-speed and phase RMS voltage-speed characteristics of the four machines: torque-speed (a); phase RMS voltage-speed (b)

It is shown that in the constant torque area, the output torque of DTP-24S is higher than that of TP-12S and TP-24S, and slightly lower than that of DTP-12S. The turning speed of the four machines is 1 500 r/min.

The phase inductance determines the performance of flux weakening. The phase inductance is greater and the constant power area is wider. For example, the d-axis inductances of DTP-24S, TP-12S, DTP-12S and TP-24S at the turning speed are 2.3 mH, 6.8 mH, 3.5 mH and 4.5 mH. So, the flux-weakening performance of TP-12S and DTP-12S is better than that of DTP-24S and TP-24S.

The 2D FEM-calculated efficiency map of the four machines in the full-speed range is shown in Fig. 15. The proportion of the high-efficiency region accounting for the total region can be calculated as

$$\lambda_S = \frac{S_{\eta \geq \eta_0}}{S_{\text{total}}}, \tag{20}$$

where $S_{\eta \geq \eta_0}$ is the area of the high-efficiency region and η_0 is equal to 95%. S_{total} is the total area of the efficiency map.

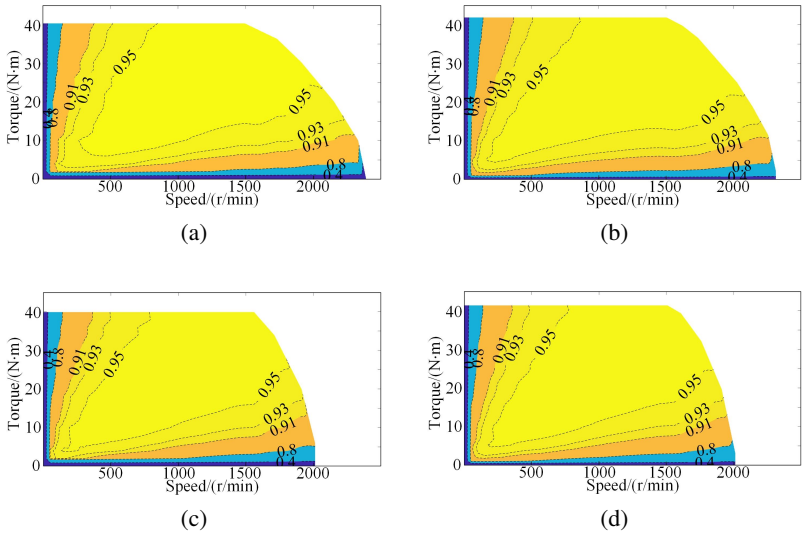

Fig. 15. 2D FEM-calculated efficiency maps of the four machines: TP-12S (a); DTP-12S (b); TP-24S (c); DTP-24S (d)

The proportion λ_S of DTP-24S, TP-12S, DTP-12S and TP-24S is 0.46, 0.47, 0.47 and 0.48. It is shown that DTP-24S has the advantage of efficiency over the other machines in the full-speed range.

4.2. Losses under SVPWM voltage supply

When the PMSM is supplied with SVPWM voltage, the armature current contains time-harmonic contents, which causes additional losses. The armature current waveforms of DTP-24S at 1 500 r/min under MTPA control are investigated by using 2D FEM field-circuit co-simulation, as shown in Fig. 16(a). Fig. 16(b) shows the harmonic analysis of phase current. The orders of main time-harmonic contents are 40 ± 4, 40 ± 2, 80 ± 1 and 80 ± 5.

Magnet ECL and core loss of the four machines are calculated by 2D FEM field-circuit co-simulation, as shown in Table 8, where p_{core} is the sum of stator and rotor core loss. AC copper loss is calculated by the sum of ohmic loss caused by each time-harmonic current. It can be seen that magnet ECL of DTP-24S is 62.0% lower than that of TP-12S and 60.9% lower than that of DTP-12S. The total losses of the four machines are almost similar.

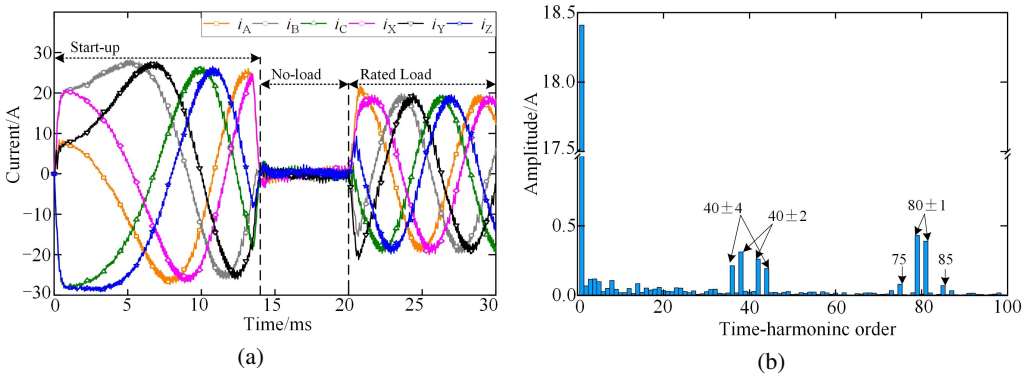

Fig. 16. Armature current of DTP-24S under MTPA control: waveforms (a); harmonic analysis (b)

Table 8. Losses of the four machines under MTPA control by 2D FEM field-circuit co-simulation

Parameter name	TP-12S	DTP-12S	TP-24S	DTP-24S
p_{mag}/W	71.82	69.84	37.92	27.29
p_{ACcu}/W	165.16	165.73	166.08	163.59
p_{core}/W	111.72	122.24	152.40	163.32
p_{total}/W	348.70	357.81	356.40	354.20

4.3. Magnet time- and space-harmonic ECL

To study magnet time- and space-harmonic ECL under SVPWM voltage supply, the time- and space-harmonic MMF is derived. The l-th time-harmonic current of phase A and X of DTP-24S is expressed as

$$\begin{cases} i_{\mathrm{A}l} = I_{l\mathrm{m}} \sin(l\omega t) \\ i_{\mathrm{X}l} = I_{l\mathrm{m}} \sin\left[l\left(\omega t - \dfrac{\pi}{6}\right)\right] \end{cases}, \tag{21}$$

where $I_{l\mathrm{m}}$ is the amplitude of the l-th time-harmonic current.

Based on (21), the MMF of phase A and X is calculated as

$$F_{\mathrm{A}l}(\theta, t) = \sin(l\omega t) \sum_{k=1,3,5,\ldots}^{\infty} \frac{8N_{\mathrm{c24S}} I_{l\mathrm{m}}}{k\pi} \sin\left(\frac{k\pi}{12}\right) \cos\left(\frac{5k\pi}{24}\right) \cos\left(k\theta - \frac{5k\pi}{24}\right), \tag{22}$$

$$F_{\mathrm{X}l}(\theta, t) = -\sin\left(l\omega t - \frac{l\pi}{6}\right) \times \sum_{k=1,3,5,\ldots}^{\infty} \frac{8N_{\mathrm{c24S}} I_{l\mathrm{m}}}{k\pi} \sin\left(\frac{k\pi}{12}\right) \cos\left(\frac{5k\pi}{24}\right) \cos\left(k\theta - \frac{k\pi}{6} - \frac{5k\pi}{24}\right). \tag{23}$$

The MMF of phases A, B, C is calculated as

$$F_{1pl}(\theta,t)=\sum_{k=1,3,5,\ldots}^{\infty}\frac{8N_{c24S}I_{lm}}{k\pi}\sin\left(\frac{k\pi}{12}\right)\cos\left(\frac{5k\pi}{24}\right)\left\{\sin\left(l\omega t+k\theta-\frac{5k\pi}{24}\right)\times\left[\frac{1}{2}+\cos\frac{2(l+k)\pi}{3}\right]+\sin\left(l\omega t-k\theta+\frac{5k\pi}{24}\right)\times\left[\frac{1}{2}+\cos\frac{2(l-k)\pi}{3}\right]\right\}. \tag{24}$$

The MMF of phases X, Y, Z is calculated as

$$F_{2pl}(\theta,t)=\sum_{k=1,3,5,\ldots}^{\infty}\frac{8N_{c24S}I_{lm}}{k\pi}\sin\left(\frac{k\pi}{12}\right)\cos\left(\frac{5k\pi}{24}\right)\times\left\{\sin\left(l\omega t+k\theta-\frac{(l+k)\pi}{6}-\frac{5k\pi}{24}\right)\times\left[\frac{1}{2}+\cos\frac{2(l+k)\pi}{3}\right]+\sin\left(l\omega t-k\theta-\frac{(l-k)\pi}{6}+\frac{5k\pi}{24}\right)\times\left[\frac{1}{2}+\cos\frac{2(l-k)\pi}{3}\right]\right\}. \tag{25}$$

The total MMF of DTP-24S is calculated by (24) and (25), as shown in (26).

$$F_{l}(\theta,t)=\sum_{k}^{\infty}\frac{16N_{c24S}I_{lm}}{k\pi}\sin\left(\frac{k\pi}{12}\right)\cos\left(\frac{5k\pi}{24}\right)\times\left\{\sin\frac{(l+k)\pi}{12}\cos\left[l\omega t+k\theta-\frac{(l+k)\pi}{12}-\frac{5k\pi}{24}\right]\times\left[\frac{1}{2}+\cos\frac{2(l+k)\pi}{3}\right]+\sin\frac{(l-k)\pi}{12}\cos\left[l\omega t-k\theta-\frac{(l-k)\pi}{12}+\frac{5k\pi}{24}\right]\times\left[\frac{1}{2}+\cos\frac{2(l-k)\pi}{3}\right]\right\}. \tag{26}$$

According to the value of k and l, the l-th time- and k-th space-harmonic MMF is derived as (27). Magnet ECL exists only when the value of harmonic MMF is not equal to zero.

$$F_{lk}(\theta,t)=\begin{cases}\dfrac{24N_{c24S}I_{lm}}{k\pi}\sin\left(\dfrac{k\pi}{12}\right)\cos\left(\dfrac{5k\pi}{24}\right)\sin\dfrac{(l+k)\pi}{12}\cos\left[l\omega t+k\theta-\dfrac{(l+k)\pi}{12}-\dfrac{5k\pi}{24}\right] & \\ \qquad l+k=3i,\qquad |l-k|\neq 3i,\qquad i=0,1,2,\ldots & \\ \dfrac{24N_{c24S}I_{lm}}{k\pi}\sin\left(\dfrac{k\pi}{12}\right)\cos\left(\dfrac{5k\pi}{24}\right)\sin\dfrac{(l-k)\pi}{12}\cos\left[l\omega t-k\theta-\dfrac{(l-k)\pi}{12}+\dfrac{5k\pi}{24}\right] & \\ \qquad l+k\neq 3i,\qquad |l-k|=3i,\qquad i=0,1,2,\ldots & \\ 0\qquad l+k\neq 3i,\qquad |l-k|\neq 3i,\qquad i=0,1,2,\ldots & \end{cases} \tag{27}$$

Based on (27), the mechanical angular velocity and frequency of the l-th time- and k-th space-harmonic MMF in the rotor reference frame can be calculated as

$$\omega_{lkr}=\left(\mathrm{sgn}\cdot\frac{l\omega}{k}-\frac{\omega}{p}\right), \tag{28}$$

$$f_{lkr}=\frac{\omega}{2\pi}\left|\mathrm{sgn}\cdot l-\frac{k}{p}\right|, \tag{29}$$

where: sgn is equal to 1 when k, l are satisfied with $l + k = 3i$ and $|l - k| \neq 3i$, while sgn is equal to -1 when k, l are satisfied with $l + k \neq 3i$ and $|l - k| = 3i$.

Table 9 shows the sgn and f_{lkr} of the time- and space-harmonic MMF in the rotor reference frame when DTP-24S is supplied with the armature current, as shown in Fig. 16(a). It is noted that phase A of the 38th and 44th time-harmonic current calculated by field-circuit co-simulation leads phase B by 120° and phase B leads phase C by 120°, while phase A calculated by (21) lags behind phase B by 120° and phase B lags behind phase C by 120°. This difference influences the sgn of harmonic MMF.

Table 9. The sgn and f_{lkr} of time- and space-harmonic MMF under SVPWM voltage supply

l	k	sgn	f_{kr} [Hz]
38	1	−1	4 775
	5	1	4 625
	11	1	4 475
	19	−1	5 225
44	1	−1	5 525
	5	1	5 375
79	5	−1	10 000
	7	1	9 700
	17	−1	10 300
	19	1	9 400
	29	−1	10 600

The magnet time- and space-harmonic ECL of DTP-12S and DTP-24S is also calculated by Ohm' law and the Fourier series of the average eddy-current density of all mesh elements, as shown in Fig. 17. It can be seen from Fig. 17 and Table 9 that the frequency of harmonic eddy-current

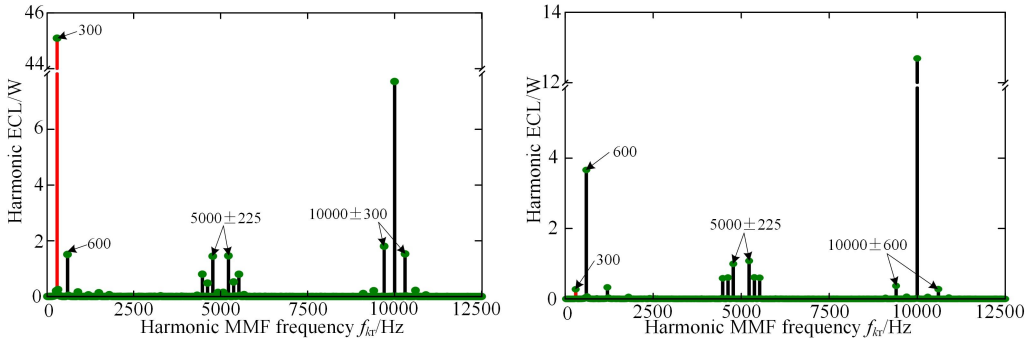

Fig. 17. Magnet time- and space-harmonic ECL distribution: DTP-12S (a); DTP-24S (b)

density corresponds to that of time- and space-harmonic MMF in the rotor reference frame. The 300 Hz harmonic ECLs of DTP-12S and DTP-24S are 45.09 W and 0.27 W, respectively. The 300 Hz harmonic ECLs are reduced greatly due to the low amplitude of 7th and 17th space-harmonic MMF. Thus, the total magnet ECL of DTP-24S is reduced greatly.

5. Conclusion

In order to reduce the armature space-harmonic MMF and magnet ECL of FSCW-PMSMs, a dual three-phase 10-pole/24-slot winding layout is proposed in this paper. Electromagnetic performances of the proposed machine under rated sinusoidal current supply and SVPWM voltage supply are investigated. The main conclusions can be summarized as follows.

1. The proposed dual three-phase 10-pole/24-slot winding can cancel the harmonics of order $1, 11, 13, \ldots, 12v \pm 1$ $(v = 1, 2, 3, \ldots)$, and reduce 7th and 17th space harmonics by 86.95% when compared with DTP-12S.
2. Under rated sinusoidal current supply, the proposed machine has better performances of no-load line back-EMF, torque and electromagnetic efficiency. The total ECL of the proposed machine is reduced by 90.46% when compared with DTP-12S, due to the reduction of 7th and 17th space harmonics.
3. The output torque in the constant torque area and efficiency in the full-speed range of DTP-24S are better, but the flux-weakening performance is poorer due to lower phase inductance. Under SVPWM voltage supply and MTPA control, the magnet ECL of DTP-24S is 60.9% lower than DTP-12S due to the reduction of 7th and 17th space harmonics.

Acknowledgements

This work is supported in part by the National Science Foundation of China under Grant 51907052, in part by the China Postdoctoral Science Foundation under Grant 2017M621606, and in part by the Jiangsu Province Postdoctoral Science Foundation under Grant 2016-416109.

References

[1] Ma W.M., Wang D., Cheng S.W., Chen J.Q., *Common basic scientific problems and development of leading-edge technology of high performance motor system*, Proceedings of the Chinese Society of Electrical Engineering, vol. 36, no. 8, pp. 2025–2035 (2016), DOI: 10.13334/j.0258-8013.pcsee.2016.08.001.

[2] Gan X.G., Fan Z.N., Li J.C., *Analysis of electromagnetic performance of the interior permanent magnet brushless DC motor with stator slot skewed structure based on quasi-3D moving electromagnetic-field circuit coupling calculation*, Archives of Electrical Engineering, vol. 71, no. 1, pp. 159–174 (2022), DOI: 10.24425/aee.2022.140203.

[3] Zhang L., Zhu X.Y., Zuo Y.F., *Overview of fault-tolerant technologies of rotor permanent magnet brushless machine and its control system for electric vehicles*, Proceedings of the Chinese Society of Electrical Engineering, vol. 39, no. 6, pp. 1792–1802 (2019), DOI: 10.13334/j.0258-8013.pcsee.181699.

[4] Qiu H.B., Zhang S.B., *Rotor optimization of axial-radial flux type synchronous machine based on magnetic flux leakage*, Archives of Electrical Engineering, vol. 70, no. 3, pp. 551–566 (2021), DOI: 10.24425/aee.2021.137573.

[5] Palangar M.F., Soong W.L., Bianchi N., Wang R.-J., *Design and Optimization Techniques in Performance Improvement of Line-Start Permanent Magnet Synchronous Motors: A Review*, IEEE Transactions on Magnetics, vol. 57, no. 9, pp. 1–14 (2021), DOI: 10.1109/TMAG.2021.3098392.

[6] Palangar M.F., Soong W.L., Mahmoudi A., *Outer and Inner Rotor Line-Start Permanent-Magnet Synchronous Motors: An Electromagnetic and Thermal Comparison Study*, IEEE Energy Conversion Congress and Exposition (ECCE), pp. 4226–4233 (2021), DOI: 10.1109/ECCE47101.2021.9595574.

[7] Vidanalage B.D.S.G., Mukundan S., Li W.L., Kar N.C., *An Overview of PM Synchronous Machine Design Solutions for Enhanced Traction Performance*, International Conference on Electrical Machines (ICEM), pp. 1697–1703 (2020), DOI: 10.1109/ICEM49940.2020.9270882.

[8] Bonthu S.S.R., Islam M.Z., Choi S., *Performance Review of Permanent Magnet assisted Synchronous Reluctance Traction Motor Designs*, IEEE Energy Conversion Congress and Exposition (ECCE), pp. 1682–1687 (2018), DOI: 10.1109/ECCE.2018.8558230.

[9] Bao X.H., Liu J.W., Sun Y., Wu C.J., *Review and prospect of low-speed high-torque permanent magnet machines*, Transactions of China Electrotechnical Society, vol. 34, no. 6, pp. 1148–1160 (2019), DOI: 10.19595/j.cnki.1000-6753.tces.171743.

[10] Fan X.G., Zhang B., Qu R.H., Li D.W., Li J., Huo Y.-S., *Comparative thermal analysis of IPMSMs with integral-slot distributed-winding (ISDW) and fractional-slot concentrated-winding (FSCW) for electric vehicle application*, IEEE Transactions on Industry Applications, vol. 55, no. 4, pp. 3577–3588 (2019), DOI: 10.1109/TIA.2019.2903187.

[11] Fornasiero E., Bianchi N., Bolognani S., *Slot harmonic impact on rotor losses in fractional-slot permanent-magnet machines*, IEEE Transactions on Industrial Electronics, vol. 59, no. 6, pp. 2557–2564 (2012), DOI: 10.1109/TIE.2011.2168794.

[12] Tang R.Y., Chen P., Tong W.M., Han X.Y., *Analytical calculation of eddy current loss accounting for eddy current reaction*, Transactions of China Electrotechnical Society, vol. 30, no. 24, pp. 1–10 (2015), DOI: 10.19595/j.cnki.1000-6753.tces.2015.24.001.

[13] Sun Q.G., Deng Z.Q., Zhang Z.M., *Analytical calculation of rotor eddy current losses in high speed permanent magnet machines accounting for influence of slot opening*, Transactions of China Electrotechnical Society, vol. 33, no. 9, pp. 1994–2004 (2018), DOI: 10.19595/j.cnki.1000-6753.tces.170245.

[14] Yokoi Y., Higuchi T., *Stator slitting of 12-Slot 10-Pole concentrated winding motors*, IEEE Transactions on Industry Applications, vol. 54, no. 5, pp. 4377–4385 (2018), DOI: 10.1109/TIA.2018.2846591.

[15] Dajaku G., Xie W., Gerling D., *Reduction of low space harmonics for the fractional slot concentrated windings using a novel stator design*, IEEE Transactions on Magnetics, vol. 50, no. 5, pp. 1–12 (2014), DOI: 10.1109/TMAG.2013.2294754.

[16] Wang Y.H., Ma J.G., Liu C.C., Lei G., Guo Y.G., Zhu J.G., *Reduction of magnet eddy current loss in PMSM by using partial magnet segment method*, IEEE Transactions on Magnetics, vol. 55, no. 7, pp. 1–5 (2019), DOI: 10.1109/TMAG.2019.2895887.

[17] Dotz B., Gerling D., *Windings with various numbers of turns per phasor*, International Electric Machines and Drives Conference (IEMDC), pp. 1–7 (2017), DOI: 10.1109/IEMDC.2017.8002007.

[18] Alberti L., Bianchi N., *Theory and design of fractional-slot multilayer windings*, IEEE Transactions on Industry Applications, vol. 49, no. 2, pp. 841–849 (2013), DOI: 10.1109/TIA.2013.2242031.

[19] Abdel-Khalik A.-S., Ahmed S., Massoud A.-M., *Effect of multilayer windings with different stator winding connections on interior PM machines for EV applications*, IEEE Transactions on Magnetics, vol. 52, no. 2, pp. 1–7 (2016), DOI: 10.1109/TMAG.2015.2495301.

[20] Oleschuk V., Grandi G., *Six-phase motor drive supplied by four voltage source inverters with synchronized space-vector PWM*, Archives of Electrical Engineering, vol. 60, no. 4, pp. 445–458 (2011), DOI: 10.2478/v10171-011-0037-0.

[21] Chen Z.F., Xing N., Ma H.Z., Li Z.X., Zhang H.Y., *Analytical modeling and analysis of magnet harmonic loss in fractional slot permanent-magnet machines*, Transactions of China Electrotechnical Society, vol. 37, no. 14, pp. 3514–3527 (2022), DOI: 10.19595/j.cnki.1000-6753.tces.210112.

[22] Chen J., Wang Z., Wang Y.-B., Cheng M., *Analysis and control of NPC-3L inverter fed dual three-phase PMSM drives considering their asymmetric factors*, Journal of Power Electronics, vol. 17, no. 6, pp. 1500–1511 (2017), DOI: 10.6113/JPE.2017.17.6.1500.

[23] Chen Q.X., Liang D.L., Jia S.F., Wan X.B., *Analysis of multi-phase and multi-layer factional-slot concentrated-winding on PM eddy current loss considering axial segmentation and load operation*, IEEE Transactions on Magnetics, vol. 54, no. 11, pp. 1–6 (2018), DOI: 10.1109/TMAG.2018.2841874.

[24] Islam M.-S., Kabir M.-A., Mikail R., Husain I., *A systematic approach for stator MMF harmonic elimination using three-layer fractional slot winding*, IEEE Transactions on Industry Applications, vol. 56, no. 4, pp. 3516–3525 (2020), DOI: 10.1109/TIA.2020.2984195.

[25] Islam M.-S., Kabir M.-A., Mikail R., Husain I., *Space-shifted wye–delta winding to minimize space harmonics of fractional-slot winding*, IEEE Transactions on Industry Applications, vol. 56, no. 3, pp. 2520–2530 (2020), DOI: 10.1109/TIA.2020.2975766.

[26] Abdel-Khalik A.-S., Ahmed S., Massoud A.-M., *A six-phase 24-Slot/10-Pole permanent-magnet machine with low space harmonics for electric vehicle applications*, IEEE Transactions on Magnetics, vol. 52, no. 6, pp. 1–10 (2016), DOI: 10.1109/TMAG.2016.2535230.

[27] Sun H.Y., Wang K., Zhu S.S., Liu C., *Performance comparisons of fractional slot surface-mounted permanent magnet machines with slot-harmonic-only windings*, IEEE Transactions on Energy Conversion, vol. 36, no. 2, pp. 995–1004 (2021), DOI: 10.1109/TEC.2020.3027007.

[28] Reddy P.B., Huh K., EL-Refaie A.M., *Generalized approach of stator shifting in interior permanent-magnet machines equipped with fractional-slot concentrated windings*, IEEE Transactions on Industrial Electronics, vol. 61, no. 9, pp. 5035–5046 (2014), DOI: 10.1109/TIE.2013.2297515.